# A Condensed History Approach to X-Ray Dark Field Effects in Edge Illumination Phase Contrast Simulations

N. Francken[1,2], J. Sanctorum[1,2], J. Renders[1,2], P. Paramonov[1,2], J. Sijbers[1,2] and J. De Beenhouwer[1,2]

***Abstract*— X-ray dark field signals, measurable in many x-ray phase contrast imaging (XPCI) setups, stem from unresolvable microstructures in the scanned sample. This makes them ideally suited for the detection of certain pathologies, which correlate with changes in the microstructure of a sample. Simulations of x-ray dark field signals can aid in the design and optimization of XPCI setups, and the development of new reconstruction techniques. Current simulation tools, however, require explicit modelling of the sample microstructures according to their size and spatial distribution. This process is cumbersome, does not translate well between different samples, and considerably slows down simulations. In this work, a condensed history approach to modelling x-ray dark field effects is presented, under the assumption of an isotropic distribution of microstructures, and applied to edge illumination phase contrast simulations. It substantially simplifies the sample model, can be easily ported between samples, and is two orders of magnitude faster than conventional dark field simulations, while showing equivalent results.**

***Clinical relevance*— Dark field signal provides information on the microstructure distribution within the investigated sample, which can be applied in areas such as histology and lung x-ray imaging. Efficient simulation tools for this dark field signal aid in optimizing scanning setups, acquisition schemes and reconstruction techniques.**

## I. INTRODUCTION

X-ray phase contrast imaging (XPCI) is an active field of research because of its increased contrast to noise ratio over conventional, attenuation based x-ray imaging. This is especially true for medical applications, such as mammography, considering the low absorption contrast of x-rays in biological samples [1]. Apart from the phase contrast, many x-ray phase contrast setups provide additional information in the form of small angle x-ray scattering (SAXS) through the so-called dark field contrast. The latter contrast, which originates from x-ray refraction by unresolvable microstructures in a sample, holds potential for histology [2] and the imaging of biological samples, such as lungs, as described in [3], where results of in-vivo human lung dark field scans are presented. While these results were obtained using a grating-based interferometer [4], it is not the only XPCI setup with clinical relevance. In [5], the edge illumination (EI) setup is used to provide high definition virtual slices of breast specimens.

EI, the XPCI setup discussed in this work, employs two absorbing masks to split the x-ray beam into separate smaller *beamlets* [1]. Phase contrast is deduced from the refraction of the individual beamlets by a sample, whereas dark field is measured as the beamlet broadening. It has been shown that a geometric optics formulation can be used to describe the EI setup [6], allowing for a ray tracing model, where the phase and dark field contrasts are both generated by ray refraction. The difference is in the scale and number of structures causing the refraction. For a detectable dark field signal, a large quantity of microstructures that cannot be resolved by the imaging system is needed, as well as an adequately sensitive setup. The sensitivity is determined by factors such as the focal spot size and mask aperture width.

X-ray dark field imaging is finding its way into clinical applications. To aid this process, efficient simulation software is crucial. It provides a modelling environment to test new setups and acquisition methods, and helps develop new reconstruction techniques. Current dark field simulations require the microstructures in a sample to be explicitly modeled, with their correct sizes and spatial distributions, which quickly becomes tedious [7]. Moreover, this modelling has to be repeated for each new material or sample. Together with increasing simulation times for larger numbers of microstructures, it complicates the generation of both accurate and performant dark field simulations.

The dark field effect can be modeled through a so-called linear diffusion coefficient, analogous to the linear attenuation coefficient. Integrating this coefficient over the ray path length then yields the total amount of SAXS. This has been successfully applied to achieve quantitative computed tomography reconstructions [8]. The model has, however, not yet been applied directly to ray tracing simulations, where it can be used to simplify and speed up the simulation process.

In this work, the implementation of an efficient dark field simulation model in a recently developed CAD-projector toolbox [9] (with an open-source release planned) is presented. The model is a condensed history method [10] that combines the many refraction events along the ray path, caused by microstructures, into a single ray update. It is shown how, under the assumption of an isotropic microstructure distribution, simulations can be considerably simplified and sped up, while remaining accurate. Microstructure regions are replaced by identically shaped regions containing no structure, but which have a new dark field parameter acting as a linear diffusion coefficient, representing the average microstructure size and number density. The condensed history dark field effect, modeled as a ray update, is applied at interfaces between different dark field regions and models the cumulative dark field effect through a whole region.

[1]imec-Vision Lab, Dept. Physics, University of Antwerp, Belgium
[2]DynXlab: Center for 4D Quantitative X-ray Imaging & Analysis, Antwerp, Belgium
Corresponding author: nicholas.francken@uantwerpen.be

## II. METHODS

### A. Edge Illumination

Edge illumination is a phase contrast setup that utilizes two masks, each with slit-shaped apertures and fabricated out of a highly absorbing material, commonly gold. The pitch of the apertures is equal to (a multiple of) the demagnified detector pixel size. One mask is placed right in front of the sample, the other mask in front of the detector, as illustrated in Fig. 1. The sample mask splits the x-ray cone beam into smaller *beamlets*, while the detector mask shields the edges of every pixel, leaving only the central part of every pixel column uncovered. The aperture size is on the order of tens of micrometers.

To perform phase contrast imaging, the sample mask is stepped laterally with respect to the detector mask, i.e., perpendicular to the aperture orientation. By measuring the intensity as a function of the mask displacement, a so called illumination curve (IC) is constructed for every pixel. This IC can be measured both with (sample IC) and without (flatfield IC) a sample present. Assuming the IC can be approximated by a Gaussian fit [11], the three different contrasts (attenuation, phase and dark field) can then be retrieved from the fitting parameters. Dark field is related to an increase in width of the sample IC compared to the flatfield IC.

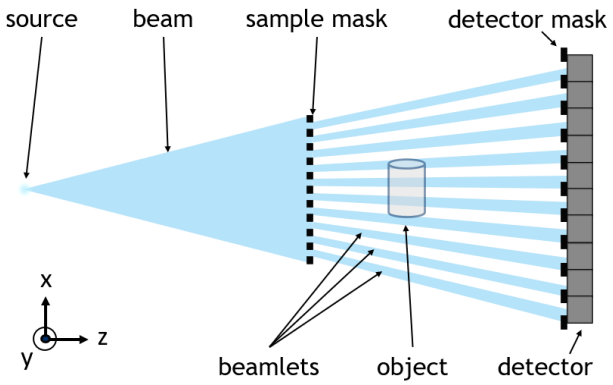


Fig. 1. A standard edge illumination setup (not to scale).

### B. Simulation framework

The simulation software that is used, is a recently developed toolbox for the efficient simulation of x-ray radiographs of CAD models [9], with an upcoming open-source release planned. The toolbox includes different state-of-the-art projectors, out of which one of the ray tracing projectors was used to generate the simulations. The toolbox models x-ray attenuation through the application of the Beer-Lambert law, and uses Snell's law at interfaces to model x-ray refraction. The EI masks and the sample(s) are provided in the form of triangular surface meshes. The sample mask movement is implemented through simple mesh translations. Monochromatic simulations are considered, where each mesh has a single linear attenuation coefficient and refractive index associated to it. The former is used, together with the ray path length, to calculate ray attenuation and the latter to determine ray refraction. Dark field is then simulated by introducing a sample containing microstructures, which causes repeated ray refraction.

In this work, a dark field parameter, functioning as a linear diffusion coefficient, is linked to each mesh. The parameter represents the average SAXS power in a mesh, and integrating it over the ray path length yields the total amount of scattering within each mesh. The scattering results in an angular broadening of the beamlets, giving the dark field parameter a per-distance unit of rad$^2$/mm (where the actual distance unit is chosen arbitrarily). With this parameter, samples can be fully described by their bounding surfaces, without the need for an explicit internal microstructure. Similar to other condensed history methods, a single dark field update is then applied to each ray when it exits a mesh. The magnitude of this update depends on the dark field parameter $p_{\mathrm{DF}}$, integrated over the ray path length $l$. The plane perpendicular to the ray direction $\vec{r}_{\mathrm{old}}$ is calculated, and two orthogonal unit vectors describing the plane are constructed. The components of these vectors are then scaled with samples from a zero-mean normal distribution $\mathcal{N}(0, \sin^2(\sigma_{\mathrm{DF}}))$, where $\sigma^2_{\mathrm{DF}} = l\ p_{\mathrm{DF}}$ and the sine converts the angle into a distance measure, resulting in the update vectors $\vec{u}$ and $\vec{v}$. The ray $\vec{r}_{\mathrm{old}}$ is pushed along $\vec{u}$ and $\vec{v}$, resulting in the new ray direction $\vec{r}_{\mathrm{new}}$, as illustrated in Fig. 2. The magnitude and direction of the update vectors mimics the beam broadening that is normally caused by repeated ray refraction in microstructures. The normal distribution variance is the dark field parameter integrated over the ray path length through the mesh. Note that, apart from the dark field update, refraction still happens at the mesh boundaries and is applied after the dark field update. We can thus write the dark field update as

$$\vec{r}_{\mathrm{new}} = \vec{r}_{\mathrm{old}} + \vec{u} + \vec{v} \quad . \tag{1}$$

## III. EXPERIMENTS

The EI setup was modeled as a parallel beam setup by placing the source $20\,\mathrm{m}$ away from the sample. The detector was placed $60\,\mathrm{cm}$ behind the sample, and the sample and detector masks were placed 5 cm before the sample and detector, respectively. The pixel size was $150\,\mu\mathrm{m} \times 150\,\mu\mathrm{m}$ and the apertures for both masks had a projected width of $30\,\mu\mathrm{m}$ at the detector plane. Both masks were $225\,\mu\mathrm{m}$ thick

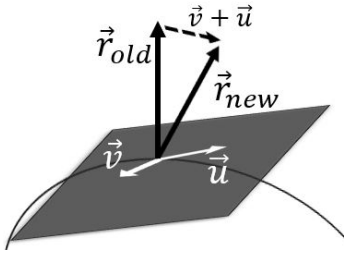


Fig. 2. Sketch of the dark field update.

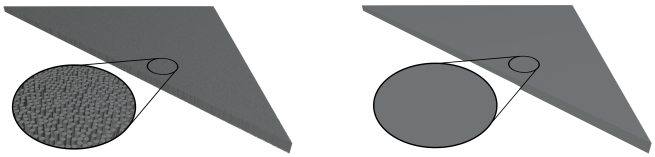

(a) Reference mesh. (b) Solid mesh.

Fig. 3. Two wedge surface meshes used in the first simulation experiment. Three different realizations of the reference mesh were generated, using the same microstructure parameters.

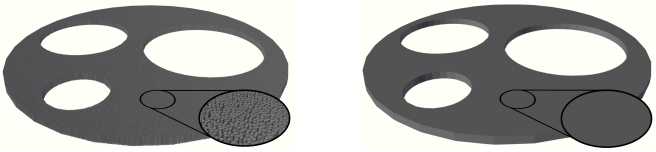

(a) Reference mesh. (b) Solid mesh.

Fig. 4. Two circular surface meshes used in the second simulation experiment. Three different realizations of the reference mesh were generated, using the same microstructure parameters.

and made of gold. The sample mask was moved along 11 equally spaced phase steps in the $[-40\,\mu\text{m}, 40\,\mu\text{m}]$ interval, relative to perfect alignment with the detector mask.

To test the condensed history approach to dark field modelling, two wedge meshes were created, as shown in Fig. 3. The first wedge was composed of approximately 245,000 small cylindrical microstructures and served as a reference. The second was a solid wedge within which there were no microstructures. The microstructures in the first mesh had a radius of $10\,\mu\text{m}$, giving a total porosity of approximately 77%. The bounding box dimensions for both meshes were 20 by 20 by 0.5 mm$^3$, with the thickness monotonically increasing from 0 to 20 mm.

After the calibration of the dark field parameter using the wedge meshes, a microstructure and solid version of a circular sample containing three holes was generated (see Fig. 4). The version with explicit microstructures used the same structure distribution as the reference wedge, while the solid sample used the same dark field parameter as was found for the solid wedge. Both circle meshes had a diameter of $20\,\text{mm}$, while the holes had an approximate diameter of 9, 7 and 4 mm. The same acquisition setup was used as for the wedge samples.

For the solid material in both samples, the linear attenuation coefficient $\mu$ and the decrement from unity $\delta$ of the complex refractive index were $\mu$ = 0.38 cm$^{-1}$ and $\delta$ = $2.56\times10^{-7}$, which corresponds to water at 30 keV. The microstructure reference wedge had a dark field parameter of zero, as here ray refraction in the microstructures caused the dark field signal. The slope of the observed reference dark field signal as function of the wedge thickness was fitted, which was then used to calibrate the dark field parameter in the solid wedge mesh. To reduce local variation effects in the signal of the reference dark field wedge, three different realizations of the mesh were created and their resulting

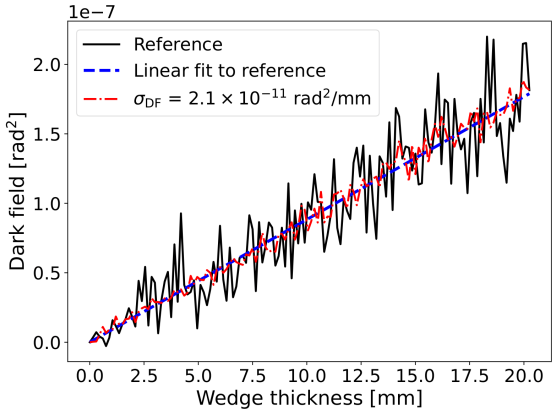


Fig. 5. The dark field signal and linear fit for the averaged reference wedge, and the dark field signal of the parameterized solid wedge mesh in Fig. 3.

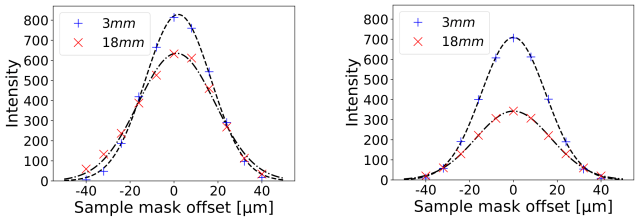


(a) Reference ICs (b) Condensed history ICs

Fig. 6. The sample points and fitted ICs for the reference (a) and parameterized solid (b) wedge meshes at 3 mm and 18 mm thickness.

signals were averaged. The simulations were run on an NVIDIA RTX 3070 GPU, using OptiX version 7.4.

## IV. RESULTS & DISCUSSION

The dark field signal, for both the averaged reference meshes and the parameterized mesh, is given in Fig. 5. As it is measured as an angular broadening of the beamlets generated by the sample mask, it has units of rad$^2$. Fig. 5 also shows a linear fit to the reference dark field signal, the slope of which was used to determine the dark field parameter in the solid wedge mesh. The dark field parameter found this way is $2.1\times10^{-11}$ rad$^2$/mm.

The sample points and fitted ICs at a thin (3 mm) and a thick (18 mm) region of the wedge are shown in Fig. 6a for a reference wedge and Fig. 6b for the condensed history approach on the parameterized solid wedge. Even though the dark field signal is almost the same, the ICs look different, because the current implementation of the condensed history update does not take into account the difference in porosity between the reference wedge and the solid wedge. The attenuation in the solid wedge is thus overestimated resulting in a lower IC, which can be compensated for by introducing an effective attenuation coefficient for the solid mesh that takes the porosity into account.

For the reference wedge mesh, where the dark field is simulated as a large number of refraction events, the simulation took 765 seconds, while the condensed history

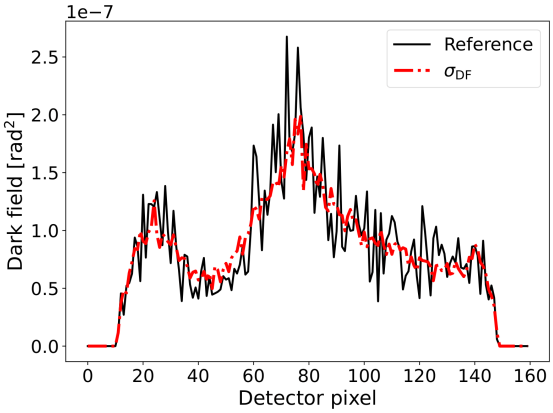


Fig. 7. The dark field signal for the circular explicit microstructure and parameterized solid meshes in Fig. 4.

version of the simulation, where a single update is applied to each ray when it exits the solid wedge mesh, took only 2.1 seconds, resulting in approximately a 364 times simulation speed increase. This speed up is expected to increase even more for more complex meshes, as the simulation time for samples with explicit microstructures scales with the number of microstructures.

The dark field parameter found in the wedge mesh experiment ($\sigma_{DF} = 2.1\times10^{-11}$ rad$^2$/mm) is validated using the second sample (see Fig. 4), for which the resulting line profiles are shown in Fig. 7. Again, three realizations of the explicit microstructure mesh are used to average the high variance dark field signal. Good agreement is found between the two profiles, indicating that the introduced condensed history model can accurately approximate the dark field effects.

The second experiment shows that, once calibrated, the dark field parameter can be freely ported between different samples. However, this is only possible when the microstructure remains the same. To model a sample with a different microstructure, the parameter has to be recalculated. As opposed to attenuation coefficients and refractive indices, tables for the linear diffusion coefficient are currently not available. A possible approach could be to estimate the linear diffusion coefficient for a limited set of samples containing microstructures of different sizes. Linear diffusion coefficients for other samples can then be interpolated/extrapolated from these results.

The simulation model includes some assumptions. First, the nature of the dark field update assumes that all the ray refraction events can be bundled into a single update. Moreover, it is assumed that a ray does not change direction within the dark field mesh, but only when it exits the mesh. In reality, the ray will exit the dark field mesh both with a different direction and at a different location, due to direction updates along the path. The condensed history update could thus also be modeled as a combined change in ray intersection point and ray direction. Lastly, the current implementation implicitly assumes the microstructures to have an isotropic distribution, i.e. that the dark field parameter is independent of the viewing angle. In standard CT or radiography, this corresponds with a distribution of equal shape spheres (or upright cylinders along the rotation axis). However, microstructures might be elongated along a specific direction (e.g. fiber bundles). In this case, the dark field signal has a directional dependence [12], and should be described by a tensor. The specific dark field update for a ray going through a sample containing such anisotropic microstructure will then depend on the projection of the dark field tensor on the ray direction.

## V. CONCLUSIONS

A condensed history method for modelling dark field simulations is demonstrated. Although its application is shown for edge illumination, it can be introduced in any ray tracing based phase contrast simulation tool. It is shown that the condensed history update can be calibrated to give equivalent results compared to a reference mesh containing explicitly modeled microstructures. This new dark field modelling approach leads to a simplified and more memory efficient representation of the sample, and speeds up simulations by two orders of magnitude.

## ACKNOWLEDGMENT

This research is funded by the Research Foundation Flanders (FWO) projects G090020N, G094320N, and FoodPhase (S003421N). Jens Renders is an SB PhD fellow at the FWO, grant no. 1SA2920N.

## REFERENCES

[1] Olivo, A., "Edge-illumination X-ray phase-contrast imaging," in Journal of Physics: Condensed Matter, vol. 33, no. 36, pp. 363002, 2021.
[2] Shimao D., et al., "X-ray Dark-Field Imaging (XDFI)-a Promising Tool for 3D Virtual Histopathology," in Molecular Imaging and Biology, vol. 23, no. 4, pp. 481-494, 2021.
[3] Urban, T., et al., "Qualitative and Quantitative Assessment of Emphysema Using Dark-Field Chest Radiography," in Radiology, vol. 303, no. 1, pp. 119-127, 2022.
[4] Pfeiffer F., et al., "Hard-X-ray dark-field imaging using a grating interferometer," in Nature Materials, vol. 7, no. 2, pp. 134-137, 2008.
[5] Massimi, L., et al., "Volumetric High-Resolution X-Ray Phase-Contrast Virtual Histology of Breast Specimens With a Compact Laboratory System," in IEEE Transactions on Medical Imaging, vol. 41, no. 5, pp. 1188-1195, 2022.
[6] Munro, P. R. T., Ignatyev, K., Speller, R. D., and Olivo, A., "The relationship between wave and geometrical optics models of coded aperture type X-ray phase contrast imaging systems," in Optics Express, vol. 18, no. 5, pp. 4103-4117, 2010.
[7] Sanctorum, J., De Beenhouwer, J., and Sijbers, J., "X-ray phase contrast simulation for grating-based interferometry using GATE," in Optics Express, vol. 28, no. 22, pp. 33390–33412, 2020.
[8] Bech, M. et al., "Quantitative X-ray dark-field computed tomography," in Physics in Medicine & Biology, vol. 55, no. 18, pp. 5529, 2010.
[9] Paramanov, P., Renders, J., Elberfeld, T., De Beenhouwer, J., and Sijbers J., "Efficient X-ray projection of triangular meshes based on ray tracing and rasterization," in Proc. SPIE 12242, Developments in X-Ray Tomography XIV, vol. 12242, pp. 122420W , 2022.
[10] Bhan, K. and Spanier, J., "Condensed history Monte Carlo methods for photon transport problems," in Journal of Computational Physics, vol. 225, no. 2, pp. 1673-1694, 2007.
[11] Endrizzi, M. and Olivo, A., "Absorption, refraction and scattering retrieval with an edge-illumination-based imaging setup," in Journal of Physics D: Applied Physics, vol. 47, no. 50, pp. 505102, 2014.
[12] Malecki, A., et al., "X-ray tensor tomography," in Europhysics Letters, vol. 105, no. 3, pp. 38002, 2014.